Published in final edited form as:
*Nat Biotechnol*. 2017 July ; 35(7): 659–666. doi:10.1038/nbt.3906.

# Guided self-organization and cortical plate formation in human brain organoids

**Madeline A. Lancaster**[1,2], **Nina S. Corsini**[1], **Simone Wolfinger**[1], **E. Hilary Gustafson**[1], **Alex Phillips**[2], **Thomas R. Burkard**[1,3], **Tomoki Otani**[4], **Frederick J. Livesey**[4], and **Juergen A. Knoblich**[1]

[1]IMBA - Institute of Molecular Biotechnology of the Austrian Academy of Science Vienna 1030, Austria

[2]MRC Laboratory of Molecular Biology, Cambridge Biomedical Campus, Cambridge CB2 0QH, UK

[3]IMP – Institute of molecular Pathology, Vienna 1030, Austria

[4]Gurdon Institute and Department of Biochemistry, University of Cambridge, Tennis Court Road, Cambridge CB2 1QN, UK

## Abstract

Three-dimensional cell culture models have either relied on the self-organizing properties of mammalian cells1–6 or used bioengineered constructs to arrange cells in an organ-like configuration7,8. While self-organizing organoids excel at recapitulating early developmental events, bioengineered constructs reproducibly generate desired tissue architectures. Here, we combine these two approaches to reproducibly generate human forebrain tissue while maintaining its self-organizing capacity. We use poly(lactide-co-glycolide) copolymer (PLGA) fiber microfilaments as a floating scaffold to generate elongated embryoid bodies. Microfilament-engineered cerebral organoids (enCORs) display enhanced neuroectoderm formation and improved cortical development. Furthermore, reconstitution of the basement membrane leads to characteristic cortical tissue architecture, including formation of a polarized cortical plate and radial units. Thus, enCORs model the distinctive radial organization of the cerebral cortex and allow for the study of neuronal migration. Our data demonstrate that combining 3D cell culture with bioengineering can increase reproducibility and improve tissue architecture.

Correspondence should be addressed to M.A.L. mlancast@mrc-lmb.cam.ac.uk or J.A.K. juergen.knoblich@imba.oeaw.ac.at.

**Data availability**
RNAseq data is available at GEO, accession number GSE80538.

**Author contributions**
M.A.L. conceived the project, planned and performed experiments and wrote the manuscript. N.S.C. performed experiments and analyzed data. S.W. and H.G. prepared samples and performed various treatments. A.P. performed cloning and prepared samples. T.R.B. performed bioinformatics analysis of RNAseq data. T.O. prepared samples and performed experiments under the supervision of F.J.L. J.A.K. supervised the project, planned and interpreted experiments, and wrote the manuscript.

**Declaration of competing financial interests**
M.A.L. and J.A.K. have filed a patent application for use of this technology in future disease modeling and toxicology testing.


Europe PMC Funders Author Manuscripts

**Keywords**

Neurogenesis; human brain development; organoid; scaffold; patterning; neuronal migration

Three-dimensional self-organizing *in vitro* tissues called organoids have the potential to revolutionize drug discovery and disease research. However, their utility has been limited by high variability, random tissue identity and incomplete morphological differentiation9,10. To identify sources of variability in brain organoids11, we examined multiple organoids from independent batches at various stages. We found that while early organoids at the embryoid body (EB) stage were virtually indistinguishable (Supplementary Fig. 1a), variation, especially between batches, became apparent during neural induction. Seven independent batches of cerebral organoids from three human pluripotent stem cell (PSC) lines revealed variable efficiency of polarized neural ectoderm formation ranging from 30–100% of organoids per batch (Supplementary Fig. 1b, c), suggesting that inconsistent neural induction efficiency might be a main source of variability.

Because most brain organoid protocols start from spherical EBs12–14, and the neuroectoderm develops on the exterior of the EB, we hypothesized that high variability may be due to low surface area to volume ratio. To test this hypothesis, we generated EBs of varying sizes by seeding different numbers of cells, from 100 to 9000 cells, because smaller-sized spheres would have a larger surface area to volume ratio. Indeed, the smaller EBs showed more relative clearing, indicative of neuroectoderm15 (Supplementary Fig. 1d). Further staining for identity markers revealed a decrease in the amount of cells with non-neuroectodermal identity, such as mesoderm and endoderm, in smaller EBs (Supplementary Fig. 1e). Upon Matrigel embedding, the smaller EBs continued to show less non-neural tissues, suggesting this could represent a route to generation of more pure neural tissues (Supplementary Fig. 1f). However, the neuroepithelial buds were smaller and there were fewer of them overall compared with those seen in larger EBs (Supplementary Fig. 1g). Furthermore, EBs generated with the smallest number of 100 cells showed increased drop-out, with some EBs failing to progress altogether. Therefore, we turned to alternative approaches to increase surface area to volume ratio while maintaining large tissues overall.

Recent studies have shown that pluripotency16 and germ layer identity during differentiation17 are influenced when PSCs are grown on micropatterned substrates. However, this approach is incompatible with current organoid protocols that require non-adhesion to a surface and extensive cell-cell contact for self-organization. We therefore sought to physically micropattern, or guide, 3D differentiation by using a floating scaffold18 to shape the organoids at the EB stage from the inside. To limit cell-scaffold contact we tested a protocol using micrometer-scale individual filaments that would contact only the innermost layer of cells of the EB (Figure 1a). We reasoned that this would allow for the formation of large tissues with increased surface area to volume while maintaining dense cell-cell contact and self-organization.

Filaments were obtained from braided fibers of PLGA 10:90 by mechanical dispersion (Supplementary Fig. 2a-c). This bio-compatible material is hydrolysed in living tissue within 8-10 weeks19. 5-10 microfilaments were collected in a random configuration at the bottom

of a low-attachment round-bottom microwell and seeded with 18,000 hPSCs, a ratio where only 5-10% of cells directly contact the filament. The hPSCs attached evenly along the length of PLGA microfilaments (Figure 1b, Supplementary Fig. 2d) or an alternative material, sea-sponge derived fibers composed of the collagen-type protein spongin (Figure 1b, Supplementary Fig. 2e). EBs generated with cellulose microfilaments (Supplementary Fig. 2f) resulted in round aggregates only partially attached to the fibers (Figure 1b). Thus, the choice of filament material is important for adherence of cells along the entire length. We pursued PLGA microfilaments further due to their availability and ease of obtaining sterile fibers (see methods).

The resulting microfilament-engineered cerebral organoids (enCORs) displayed elongated morphologies but maintained typical dense cell composition. Like spherical EBs, they progressively grew in size and exhibited clearing along the edges, eventually forming polarized neural ectoderm. However, the neural ectoderm was elongated (Figure 1c) and the efficiency of neuroectoderm formation was much improved, with consistent neural induction in all of seven independent preparations examined (Supplementary Fig. 2g-i).

Staining of early-stage microfilament-engineered EBs for germ layer markers revealed consistent generation of polarized neuroepithelium with concomitantly decreased amounts of endoderm and mesoderm identities (Figure 1d). This was in contrast with spherical organoids, which often displayed non-ectodermal identities, especially in suboptimal organoids (Figure 1e). Quantification of these identities demonstrated the reproducible formation of neuroectoderm in enCORs with an almost complete lack of non-neural tissues, whereas spheroids displayed highly variable amounts of all germ layer identities (Figure 1 f). Furthermore, expression analysis of pluripotency and germ layer markers by RT-PCR revealed a decrease in non-neural identities in enCOR organoids (Figure 1g, Supplementary Fig. 3a, b). As organoids developed, enCORs displayed fewer morphological features of these other identities, such as the formation of early fluid-filled cysts (Supplementary Fig. 3c). Furthermore, enCORs contained large lobes of brain tissue but only few regions expressing markers for endoderm and non-neural epithelia (Supplementary Fig. 3d), in contrast to spherical organoids. Thus, enCORs display more reproducible neural induction without sacrificing self-organization.

We observed that the neuroepithelial buds that formed upon Matrigel embedding were less elongated and continuous in organoids with microfilaments (Supplementary Fig. 4a). Because Wnt pathway activation has been shown to induce lateral expansion of cortical neuroepithelium20, we applied the GSK3beta inhibitor/Wnt activator CHIR99021 (CHIR) after neuroepithelial budding. This treatment resulted in larger lumens with surrounding continuous neuroepithelium (Supplementary Fig. 4b). Because Wnt signalling is also an important patterning factor21, and we sought to limit the extent of exogenous patterning, we performed treatment for only a short 3-day pulse. This treatment alone did not influence germ layer induction or overall organoid morphology (Supplementary Fig. 4c, d).

The combination of microfilament and CHIR pulse resulted in more consistent formation of large brain lobules (Figure 2a) that stained positive for the forebrain marker Foxg1 (Figure 2b) compared with spheroids. In addition, we observed reduced frequency of Otx2+

midbrain and En2+ cerebellar/hindbrain regions (Supplementary Fig. 4e). Quantification of these identities revealed more reproducible formation of forebrain in enCORs rather than other brain regions (Figure 2c). Consistent with this, enCORs displayed both dorsal and ventral forebrain regions (Supplementary Fig. 4f) with more frequent large Tbr1 and Tbr2 positive dorsal cortical regions (Figure 2d). Furthermore, enCORs displayed regions consistent with choroid plexus and hippocampus identity (Supplementary Fig. 4g, h). Thus, together with late GSK3beta inhibition, bioengineering of cerebral organoids results in reproducible formation of forebrain tissue with little contamination from other germ layers and brain regions.

To further examine the effect of the microfilament and CHIR addition we analyzed gene expression at 20 and 60 days in three enCORs and three spherical organoids (Supplementary Table 1). 20 day enCORs were enriched for GO terms “neurological system” and “multicellular organismal processes”, while other organ development terms, such as digestive tract, muscle, skeletal system and mesoderm, were decreased (Supplementary Fig. 5a). At 60 days, we observed GO term enrichment for nervous system development and transcription while digestive tract, heart, muscle skeletal system, and synaptic transmission were decreased. The decrease in synaptic genes at 60 days suggests a delay in neuronal maturation perhaps due to extended progenitor expansion upon CHIR addition. Hierarchical clustering revealed several gene clusters displaying specific patterns of differential expression (Supplementary Fig. 5b, Supplementary Fig. 6, Supplementary Table 2). Cluster 1 was upregulated in 60-day enCORs and enriched for forebrain and cortical differentiation. Clusters 4 and 5 were increased or unchanged at 20 days but decreased at 60 days and were enriched for nervous system development and synaptic transmission. Clusters 6 and 7 were decreased at 20 days and also decreased or unchanged at 60 days. They were enriched for more caudal expression such as spinal cord and hindbrain, consistent with the effect of bioengineering and CHIR addition on forebrain patterning.

We next assessed expression of specific germ layer or brain patterning markers (Supplementary Fig. 7a, b). The pluripotency markers Oct4, Klf4, and Nanog were decreased in enCORs. Neuroectodermal markers appeared unchanged whereas mesendodermal markers such as Sox17, T (Brachyury), Mixl1, and Foxa2 were decreased. Furthermore, the forebrain marker Foxg1 was sharply increased, whereas caudal markers such as En2, Gbx2 and Hox genes were decreased. Finally, dorsal forebrain markers such as Emx1, Tbr1 and Tbr2 were increased, while ventral forebrain markers were unchanged. These findings suggest a more rostral brain identity in enCORs.

Finally, we compared genes differentially expressed between 60 day spherical organoids and enCORs to gene expression in the human developing brain using Allen BrainSpan Atlas22 (Supplementary Fig. 7c). enCORs most closely matched the forebrain identities of the human brain at early gestation, specifically 8-9 weeks post-conception (Figure 2e). Spherical organoids instead showed the highest correlation with more caudal regions, specifically the thalamus and cerebellum, and showed a broader correlation with later time points (Supplementary Fig. 7c). These findings are consistent with the effect of the microfilament and CHIR addition on forebrain regional identity.

Neurons in the developing cortex *in vivo* form a dense band called the cortical plate (CP) and show radially aligned morphology. This is thought to reflect their organization into radial units23, a prerequisite for the formation of functional neuronal columns in the adult cortex 24,25. Although *in vitro* models, including organoids, properly recapitulate basal translocation of neurons and even formation of rudimentary layers reminiscent of the CP26–28, radially aligned neurons in a dense CP have not been observed, nor have radial units. This might be due to the absence of a basement membrane, which is thought to be generated by the overlying non-neural mesenchyme29,30 not present in organoids. Indeed, although staining for laminin initially revealed a well-formed basement membrane in early neuroepithelium before neurogenesis, this changed to dispersed, punctate staining, suggesting breakdown and/or failure to maintain the membrane upon generation and basal migration of neurons (Figure 3a).

To reconstitute the basement membrane, we tested exogenous extracellular matrix (ECM) components in the form of dissolved Matrigel in the media. Indeed, this treatment maintained a thick laminin-rich basement membrane that remained outside the migrating neurons (Figure 3b). Bright-field imaging revealed a band of density in cortical regions that was absent in organoids lacking dissolved ECM (Supplementary Fig. 8a). Subsequent sectioning and histological staining revealed a radialized basal layer consistent with cortical plate morphology (Figure 3c). Indeed, immunohistochemical staining revealed it was positive for the neural markers Ctip2, and Map2, with a band of lower intensity Map2 staining in cell bodies that is typical of the cortical plate *in vivo* (Figure 3d and Supplementary Fig. 8b). This treatment elicited CP formation in organoids from three independent cell lines: two hES lines and one iPS line (Supplementary Fig. 8c), and quantification of the presence of a CP revealed reproducible formation in five independent batches of enCORs while a CP was never observed in spheroids (Figure 3e).

To examine the role of Matrigel and whether it is necessary for formation of a CP, we treated with the matrix metalloprotease inhibitor GM6001 to test whether inhibition of ECM breakdown is instead sufficient for CP formation. Continuous treatment beginning at day 30 did not result in CP formation by 60 days (Supplementary Fig. 8d), suggesting that it is not simply breakdown of the initial basement membrane that inhibits CP formation in the spherical organoid method, but also a failure to maintain and expand the basement membrane with tissue growth, a hurdle overcome by addition of dissolved Matrigel. We next tested whether laminin alone, in combination with entactin, or the combination of laminin-entactin-collagen would be sufficient to recapitulate the effect of dissolved Matrigel. These treatments did not recapitulate the extent of CP formation seen with Matrigel (Supplementary Fig. 8e), suggesting other components of this complex ECM are important for basement membrane maintenance.

Recently, SFEBq forebrain organoids were combined with several modifications, including dissolving Matrigel in the media, which leads to condensation of neurons superficial to progenitor zones, reflecting an organization reminiscent of CP formation26. Furthermore, forebrain organoids and so-called cortical spheroids have both been described to exhibit features of cortical layers27,28, an organization that *in vivo* depends upon proper CP formation. We therefore compared the enCOR method with these previous approaches to

specifically test CP formation. While the SFEBq method26 displayed occasional somewhat condensed nuclei reminiscent of a CP, neither SFEBq organoids nor cortical spheroids displayed a clear, radially organized CP as seen in enCORs (Supplementary Fig. 9a, b). These data suggest that while cortical layering may occur to some extent in the earlier methods, in enCORs the events leading to proper neuronal organization may be more similar to *in vivo* development.

CP establishment *in vivo* depends upon early pioneer neurons of the preplate, which secrete Reelin to attract subsequent neurons to migrate into and split the preplate into the marginal zone (MZ) and subplate (SP). We therefore tested whether enCORs exhibited Reelin-expressing neurons, also called Cajal-Retzius cells, by staining for Reelin and calretinin. Staining for Reelin revealed strongly reactive cells in the most superficial regions, as well as more dispersed signal indicative of the fact that Reelin is a secreted factor (Figure 3f). Furthermore, calretinin staining revealed neurons in superficial regions as well as just inside the newly forming CP (Figure 3g), a pattern typical of preplate splitting *in vivo*. Staining for chondroitin sulfate proteoglycan (CSPG) further revealed splitting and establishment of MZ and SP during early CP condensation (Figure 3h). This separation was more pronounced with more developed, thicker CP. Furthermore, the CP itself widened over time and even displayed features of early cortical layering (Supplementary Fig. 9c).

The basal process of radial glial cells, which contacts the basement membrane covering the surface of the brain, acts as a scaffold for migration and orientation of neurons to allow for formation of the CP and positioning into radial units31. Nuclear staining in cortical regions of enCORs that had been sectioned evenly along the plane perpendicular to the apicobasal axis revealed linear units of radial glia and neurons aligned in a manner reminiscent of radial units (Figure 4a), a characteristic architecture not previously recapitulated *in vitro*. Furthermore, staining for phospho-vimentin, a cytoplasmic marker of dividing radial glia revealed long basal processes extending the length of the cortical wall. These basal processes were also evident upon staining for Nestin, a cytoplasmic marker of radial glia, which revealed processes with end feet that terminated on the outer surface (Figure 4b, Supplementary Fig. 10a). In contrast, spherical organoids displayed disorganized radial glial processes with terminating end feet at various locations within the tissue (Supplementary Fig. 10b).

In order to label individual cells for live imaging and morphological analyses, we next established combined electroporation and slice culture in organoids. We electroporated a GFP construct into the VZ of individual cortical lobes followed by vibratome sectioning and culture at the air-liquid interface. This allowed for marking individual radial glia, further demonstrating the long basal processes terminating superficial to the CP (Figure 4c).

Long-term live imaging of electroporated slices revealed various cell behaviors, including divisions of outer radial glia (oRG), also called basal radial glia (Figure 4d, Supplementary Video 1), which displayed mitotic somal translocation, a feature typical of oRGs *in vivo*32. Furthermore, live imaging of labelled newly generated neurons revealed typical radial migration into the intermediate zone and transient acquisition of multipolar morphology (Supplementary Fig. 10c, Supplementary Videos 2, 3) before reestablishment of radial

orientation and migration into the CP (Figure 4e, f, Supplementary Videos 1, 4, 5). Tracing of 22 individual neurons from three independent experiments further highlighted the saltatory nature of their radial migration, with long stationary periods in the intermediate zone (Figure 4g, h). Finally, we could also observe migration of putative interneurons showing tangential movement and often more than one leading process that the cell moved between (Supplementary Fig. 10d, Supplementary Video 2, 6), a feature described for tangentially migrating interneurons *in vivo*33. Establishment of labelling and long-term live imaging of slice cultures in this manner thus provides a useful tool for examination of neuronal migration and progenitor division in a human model system.

Electroporation of a membrane-targeted GFP allowed for examination of morphology of single neurons in more-developed organoids. This revealed complex dendritic morphologies and neurons with a primary dendrite typical of the pyramidal morphology of cortical neurons (Figure 4i). Furthermore, these neurons were oriented toward the MZ on the outer surface of the organoid where parallel fibers could frequently be seen. Finally, we performed calcium staining and live imaging on slice cultures, which revealed spontaneous calcium surges suggestive of neuronal activity (Supplementary Fig. 10e, Supplementary Video 7). These data point to proper positioning and maturation of cortical neurons in enCORs.

The remarkable self-organization and ability to generate the full repertoire of organ cell types have made organoids an important new model system. However, the high variability and difficulties modelling later tissue architecture has meant that subtle defects are difficult to discern. To overcome this, we tested two routes to increase the surface area-to-volume ratio: 1) decreased EB size, and 2) bioengineering using a microscale internal scaffold. Each approach could have interesting future applications. Smaller EBs may be a good route to higher-throughput analysis and drug testing, while the scaffold allows for larger continuous cortical lobes and opens the door to future development such as testing of alternative materials, adsorption of instructive factors, and even gradient generation for axis formation. Overall, we show that increasing surface area leads to reproducible neural induction, and the combination of bioengineering and self-organization allows for reliable forebrain formation without sacrificing tissue complexity. Importantly, there are still noticeable differences between different cell lines and batches, for example, in terms of tailoring the timing needed for each step. However, because enCORs show more reliable generation of forebrain and proper migration and formation of a CP, the potentially discernable phenotypes are greatly increased. Furthermore, the application of slice culture and live imaging to brain organoids allows for the study of dynamic processes in cortical development, including progenitor division and migration.

## Online Methods

### Preparation of microfilaments

Poly (lactide-co-glycolide) braided fibers of 10:90 PLGA were obtained from a commercial source as Vicryl sutures (Ethicon, size 5-0). We preferentially used violet dyed fibers to assist in visualization during dispersion and within embryoid bodies. Individual microfilaments were isolated from the braided fiber by mechanical shearing with an angled blade against a stainless steel plate, to obtain filaments of 0.5-1mm in length, and 15μm in

Europe PMC Funders Author Manuscripts

diameter. Filaments were then hydrated in embryoid body media and transferred to a 15ml conical tube for storage at 4°C. Filaments of cellulose were obtained by shaving individual fibers from a sheet of Whatman filter paper. Sea-sponge filaments were obtained by shaving fibers from a commercially available dried sea-sponge sample.

### Preparation of EBs and enCORs

Spheroids were generated with 9000 cells (unless stated otherwise) exactly as previously14 except that typical quality control and elimination of suboptimal organoids11 and batches was not performed in order to obtain the full spectrum of variability. EBs were prepared from single cell suspension following accutase treatment, as described previously11. Cell lines were human ES (H9 or H1, both from WiCell, and approved for use in this project by the U.K. Stem Cell Bank Steering Committee) or iPS cells (System Biosciences, SC101A-1), all of which have been authenticated by the provider and routinely tested negative for mycoplasma (MycoAlert, Lonza). Cells were counted and resuspended in EB media: DMEM/F12 (Invitrogen, cat. #11330-032) and 20% Knockout Serum replacement (Invitrogen, cat. #10828-028), 3% human ES quality batch-tested fetal bovine serum, 1% Glutamax (Invitrogen, cat. #35050-038), 1% MEM-NEAA (Sigma, cat. #M7145), 0.1 mM 2-mercaptoethanol, 4 ng/ml bFGF (Peprotech, cat. #100-18B), and 50μM Y-27632 ROCK inhibitor (VWR, cat. #688000-5). For enCORs, 18000 cells were added to each well of a 96-well low-attachment U-bottom plate (Sigma, cat. #CLS7007) already containing 5-10 microfilaments in EB media, and media was added to give a final volume of 150 μl per well. Based on an average hPSC cell size of 15 μm (measured from hPSC cell suspensions on EVOS microscope, Invitrogen), we calculated that 18000 cells per 5-10 fibers of maximum length 1mm would result in, at most, 5-10% of cells having direct contact to the fiber.

At day 3, half media was changed with EB media without bFGF and Y-27632. On day 5 or 6 depending on morphology (when surface tissue exhibited signs of clearing as described previously11), EBs were moved with an angled cut P200 tip to obtain a wide bore opening to 24-well low-attachment plates (Sigma, cat. #CLS3473) with neural induction media (NI) as previously described11. Media was changed every other day. On day 11, or when polarized neural ectoderm was visible on the surface as shown in Figure 1c, enCORs were transferred to a droplet of Matrigel as previously described but kept in NI media. At day 13 (2 days after Matrigel embedding), media was changed to an improved differentiation media –A (IDM-A): 1:1 of DMEM/F12 and Neurobasal (Invitrogen, cat. #21103049), 0.5% N2 supplement (Invitrogen, cat. #17502048), 2% B27 –vitamin A (Invitrogen, cat. #12587010), 0.25% insulin solution (Sigma, cat. #I9278-5ML), 50 μM 2-mercaptoethanol, 1% Glutamax, 0.5% MEM-NEAA, and 1% Penicillin-Streptomycin (Sigma, cat. #P0781). Additionally, CHIR 99021 (Tocris, cat. #4423) at 3 μM was added from day 13 to 16. Media was changed every other day and organoids were moved to an orbital shaker placed in the incubator, on day 18-20. After moving to the shaker, media was changed every 3-4 days. Importantly, shaking speed should be calculated based on the throw of the shaker. For a throw of 10 mm, speed should be 85 rpm. We noticed that an incorrect speed did not result in CP formation.

### Formation of polarized cortical plate

At day 20, media was changed to an improved differentiation +A (IDM+A): 1:1 of DMEM/F12 and Neurobasal, 0.5% N2 supplement, 2% B27 +vitamin A, 0.25% insulin solution, 50 μM 2-mercaptoethanol, 1% Glutamax, 0.5% MEM-NEAA, 1% Penicillin-Streptomycin, 0.4 mM Vitamin C, and 1.49g HEPES per 500 ml to control pH levels. Alternatively, media can be pH controlled with further bicarbonate buffering with the addition of 1mg/ml sodium bicarbonate. At day 40, media was changed to IDM+A with 1ml dissolved Matrigel per 50 ml media by slowly thawing the Matrigel on ice and adding to cold media to dissolve. For treatment with matrix metalloprotease inhibitor GM6001 (Selleck Chemicals S7157), a final concentration of 3 μM was added beginning on day 30. For testing purified ECM components, 35 ug/ml of pure laminin (Corning 354232) was added beginning on day 40, or 45 μl of high concentration laminin/entactin gel (Corning 354259) was dissolved per 5 ml media, or a 70% laminin/entactin – 30% Collagen I (Corning 354249) mixture (35 ul laminin/entactin + 25 ul collagen) was added to obtain a protein concentration comparable to final concentration of Matrigel as obtained above. For these treatments, organoids were allocated randomly to separate dishes containing the various components.

Cortical spheroids were generated as described previously27. Briefly, H9 feeder-free cells were dissociated with EDTA and intact colonies were plated in a low-attachment 6 cm dish in hES media containing small molecules as detailed in the published protocol. On day 6, media was changed to Neural Media and addition of growth factors was performed with the timing described in the protocol. Forebrain SFEBq organoids were generated as described previously26 and as in Otani et al34. Briefly, iPS cells were dissociated to single cells and 9000 cells plated per low attachment u-bottom well in cortex differentiation media containing small molecules as described in the published protocol. Media changes were performed as described and on day 19 the tissues were moved to DMEM/F12 +N2 based media with subsequent addition of FBS, heparin and Matrigel on day 35 as described. B27 was included starting at day 70, along with increased Matrigel exactly as described.

### Histological and immunohistochemical analysis

Organoids were fixed in 4% paraformaldehyde for 20 min at room temperature and washed with PBS three times for 10 min each at room temperature before allowing to sink in 30% sucrose at 4°C. The tissues were embedded and sectioned and stained as described11. Primary antibodies used were: goat anti-Brachyury (R&D Systems AF2085, 1:200), mouse anti-N-Cadherin (BD 610920, 1:500), mouse anti-E-Cadherin (BD 610182, 1:200), goat anti-Sox17 (R&D systems AF1924, 1:200), rabbit anti-Laminin (Sigma L9393, 1:500), rabbit anti-Tbr1 (Abcam ab31940, 1:300), chicken anti-Tbr2 (Millipore AB15894, 1:100), mouse anti-Map2 (Chemicon MAB3418, 1:300), rat anti-Ctip2 (Abcam, ab18465, 1:300), rabbit anti-Arl13b (Proteintech 17711-1-AP, 1:300), mouse anti-phospho-Vimentin (MBL International D076-3S, 1:250), rabbit anti-Emx1 (Sigma HPA006421, 1:200), rabbit anti-FoxG1 (Abcam ab18259, 1:200), mouse anti-Reelin, (Millipore MAB5366, 1:200), mouse anti-Calretinin (Swant 6B3, 1:100), rabbit anti-Satb2 (Abcam ab34735, 1:100), rabbit anti-Otx2 (Abcam ab21990, 1:200), goat anti-En2 (Santa Cruz Biotechnology sc-8111, 1:50), goat anti-DCX (Santa Cruz Biotechnology sc-8066,1:300), mouse anti-CSPG (Abcam

ab11570, 1:100), rabbit anti-Cux2 (Abcam ab130395, 1:200), mouse anti-Nestin (BD G11658, 1:500), mouse anti-Pax6 (DSHB, 1:100), rabbit anti-Gsh2 (Millipore ABN162, 1:500), mouse anti-Prox1 (Chemicon MAB5654, 1:200), sheep anti-TTR (AbD Serotec AHP1837, 1:100). DAPI was added to secondary antibody to mark nuclei. Secondary antibodies labeled with Alexafluor 488, 568, or 647 (Invitrogen) were used for detection. For histological analysis, sections were stained for hematoxylin/eosin followed by dehydration in ethanol and xylene and mounting in permount mountant media. Fluorescence images were acquired on a confocal microscope (Zeiss LSM 710 or 780), and bright field images were acquired on an EVOS microscope (Invitrogen). Quantification of fluorescence for germ layer identities in enCOR and spheroids was performed using Fiji by first setting threshold to obtain a binary image and remove background, then the tissue was traced in the DAPI channel and mean grey value measured for all channels. Fluorescence (mean grey value) was measured and calculated relative to DAPI. Quantification of brain region identities was performed by counting the number of lobules staining positive for the marker (Foxg1, Otx2, or En2) as a ratio of the total number of lobules visible by DAPI staining.

## Statistical analyses

Statistical analysis of quantifications performed from imaging data was performed using Student's two-tailed *t*-test for significance, and the data was tested for normality by plotting a histogram of the distribution for each dataset. Variance was similar between sets of data except where stated in the figure legend. Since this was the first quantitative investigation of variability in brain organoids, power calculation was not feasible due to a lack of information about population variability. Therefore, all available organoids were used for the experiments, such that the sample size for each treatment/experiment was the maximum available organoids in culture at the time. For quantifications of CP presence and identity, samples were given IDs that masked their identity and quantifications were done blinded.

## Electroporation of organoids and live imaging

Electroporation of pmax-GFP construct (Lonza) or an integrating farnesylated GFP was performed as described previously14. For pmax-GFP, 4 μl of 250ng/μl were injected into several ventricular spaces followed by electroporation. The integrating farnesylated GFP (pT2-CAG-fGFP) was generated by first isolating the CAG promoter from the pCAG-GFP plasmid35 (a gift from Connie Cepko, Addgene plasmid # 11150) using FastDigest CsiI (Thermofisher FD2114) and FastDigest BshTI (Thermofisher FD1464) and inserting this sequence into the pT2/HB transposon donor plasmid (a gift from Perry Hackett, Addgene plasmid # 26557). This plasmid was modified so that it included additional restriction sites and attR sites that would allow the insertion of sequences using Gateway cloning. To generate the farnesylated EGFP, the pENTR-EGFP2 plasmid36 (a gift from Nathan Lawson, Addgene plasmid # 22450) was linearized using EcoRI-HF (NEB R3101) and HindIII-HF (NEB R3104) and the farnesylation sequence was inserted in-frame immediately downstream of the GFP sequence. The farnesylated GFP was then cloned into the above pT2-CAG-pDest using Gateway cloning (Thermofisher). Sleeping beauty transposase plasmid was generated by cloning the SB100X transposase (pCMV(CAT)T7-SB10037 was a gift from Zsuzsanna Izsvak, Addgene plasmid #34879) into the pCAGEN plasmid with CAG promoter (pCAGEN35 was a gift from Connie Cepko, Addgene plasmid # 11160).

Electroporation was performed by injecting 80 ng/μl pT2-Cag-fGFP and 240 ng/μl pCAGEN-SB100X. For neuronal morphology analysis, samples were fixed 36 days after electroporation of the fGFP and analyzed by sectioning and immunohistochemistry as above.

Slice culture was performed using a modification of an *ex vivo* protocol38. Samples were embedded in 3% low-melting point agarose and sectioned on a vibratome to collect 300 μm sections on the air side of organotypic culture inserts (Millipore) inside a 3 cm coverglass bottomed dish containing 1 ml serum-supplemented media: DMEM, 10% FBS, 0.5% (w/v) glucose, supplemented with penicillin-streptomycin. Sections were cultured for 1 hour before changing the media to serum-free media: DMEM, 1:50 B27+A, 0.5% (w/v) glucose, glutamine and penicillin-streptomycin. The slices were left to flatten and equilibrate overnight before imaging over several days using a Zeiss 780 and incubation chamber with 7% $CO_2$ at 37°C. For this long-term imaging, HEPES (25 mM final) was added for pH buffering. Tracing of neuronal migration was performed using the Fiji plugin MTrackJ.

Calcium imaging was performed as previously described14 using Fluo-4 Direct (Life Technologies) on slice cultures. Frames were analyzed in ImageJ and progressive increasing intensity was corrected by using the Bleach Correction function on frames in reverse order. Individual cell traces were performed by outlining specific cells as regions of interest and mean grey value measured. $\Delta F/F$ was calculated as follows: (mean grey value – minimum grey value)/minimum grey value.

## RT-PCR analysis of gene expression

Three organoids for each condition were collected in Trizol reagent (Thermo Fisher) and RNA isolated according to manufacturer. DNA was removed using DNA-Free kit (Ambion) and reverse strand cDNA synthesis was performed using Superscript III (Invitrogen). PCR was performed using primers for a panel of pluripotent and germ layer identities (R&D systems, SC012).

## RNA-seq analysis

Three individual H9 organoids for each condition were collected at the indicated time points. RNA was isolated using Arcturus PicoPure RNA Isolation Kit (Thermo Fisher Scientific, cat. #KIT0204) (20 days timepoint) or Trizol Reagent (Thermo Fisher Scientific, cat. # 15596018) (60 days timepoint) according to the manufacturer's instructions. RNA concentration and integrity was analysed using RNA 6000 Nano Chip (Agilent Technologies, cat. #5067-1511). RNA was enriched for mRNA using Dynabeads mRNA Purification Kit (Thermo Fisher Scientific, cat. # 61006). Libraries were prepared using NEBNext Ultra Directional RNA Library Prep Kit for Illumina (NEB, cat. # E7420L). Barcoded samples were multiplexed and sequenced 50bp SE on a HighSeq2500 (Illumina). Sample preparation and sequencing was performed at the VBCF NGS Unit (www.vbcf.ac.at).

The strand specific reads were screened for ribosomal RNA by aligning with BWA (v0.6.1)39 against known rRNA sequences (RefSeq). The rRNA subtracted reads were aligned with TopHat (v1.4.1)40 against the Homo sapiens genome (hg38) and a maximum

of 6 mismatches. Maximum multihits was set to 1 and InDels as well as Microexon-search was enabled. Additionally, a gene model was provided as GTF (UCSC, 2015_01, hg38). rRNA loci were masked on the genome for downstream analysis. Aligned reads were subjected to FPKM estimation with Cufflinks (v1.3.0)41,42. In this step bias detection and correction was performed. Furthermore, only those fragments compatible with UCSC RefSeq annotation (hg38) of genes with at least one protein-coding transcript were allowed and counted towards the number of mapped hits used in the FPKM denominator. Furthermore, the aligned reads were counted with HTSeq (0.6.1p1) and the genes were subjected to differential expression analysis with DESeq2 (v1.6.3)43.

GO term enrichment analysis was performed on genes with an adjusted *p* value <0.1 and absolute log2fc value >1 in at least one of the conditions (20 day or 60 day, spheroid or enCOR). Each set of differentially expressed genes were analysed using Pantherdb.org for GO Slim biological process enrichment and fold enrichment for terms as well as multi-test corrected *P*-value (plotted as –log10(*P*value) (Supplementary Table 1).

For hierarchical cluster analysis, genes were sorted based on their similarity of log2fc values by means of Ward hierarchical clustering using heatmap.2 of the gplots package in R. Cutree function gave the 7 clusters used for subsequent GO term analysis. Gene lists were fed into Pantherdb.org for GO Biological Process Complete, yielding a large list of redundant terms. Therefore, in order to remove redundancy, we narrowed the list using GO Trimming and a cutoff of terms with fold enrichment value >2 yielding the list of GO terms that were plotted by fold enrichment value and –log10(*P*value) (Supplementary Table 2). Individual tracks were visualized using Integrative Genomics Viewer IGV_2.3.68 (Broad Institute).

For comparison to Allen BrainSpan human transcriptome dataset, the RPKM expression values of Brainspan were downloaded (http://www.brainspan.org/static/download.html). FPKM values were filtered for differential expression in the 60d time-points (padj < 0.1) and joined with Brainspan via the gene symbols. The similarity of expression was compared by the rank of the expressed gene via Spearman correlation. The heatmap of Spearman coefficient for each region at fetal time points was generated using heatmap.2 without hierarchical clustering. The list was manually ordered according to anterior-posterior regional position and separated into four developmental stages.

## Supplementary Material

Refer to Web version on PubMed Central for supplementary material.

## Acknowledgments

We thank members of the Lancaster lab for helpful discussion and technical support, especially S. Giandomenico and M. Sutcliffe, as well as A.G. Gianni for sea sponge sample. We also thank members of the Knoblich lab for insight and technical help, particularly A. Peer. M.A.L. was funded by a Marie Curie Postdoctoral fellowship, and work in M.A.L.'s laboratory is supported by the Medical Research Council (MC_UP_1201/9). N.S.C. was funded by an EMBO long-term fellowship and a Deutsche Forschungsgemeinschaft research fellowship (DFG CO 1324/1-1). Work in J.A.K.'s laboratory is supported by the Austrian Academy of Sciences, the Austrian Science Fund (grants I_1281-B19 and Z_153_B09), and an advanced grant from the European Research Council.

## References


1. Rookmaaker MB, Schutgens F, Verhaar MC, Clevers H. Development and application of human adult stem or progenitor cell organoids. Nature Reviews Nephrology. 2015; 11:546–554. [PubMed: 26215513]
2. Fatehullah A, Tan SH, Barker N. Organoids as an in vitro model of human development and disease. Nat Cell Biol. 2016; 18:246–254. [PubMed: 26911908]
3. Yin X, et al. Engineering Stem Cell Organoids. Cell Stem Cell. 2016; 18:25–38. [PubMed: 26748754]
4. Dedhia PH, Bertaux-Skeirik N, Zavros Y, Spence JR. Organoid Models of Human Gastrointestinal Development and Disease. Gastroenterology. 2016; 0
5. Sasai Y. Next-Generation Regenerative Medicine: Organogenesis from Stem Cells in 3D Culture. Cell Stem Cell. 2013; 12:520–530. [PubMed: 23642363]
6. Lancaster MA, Knoblich JA. Organogenesis in a dish: Modeling development and disease using organoid technologies. Science. 2014; 345:1247125–1247125. [PubMed: 25035496]
7. Langer R, Vacanti J. Advances in tissue engineering. Journal of Pediatric Surgery. 2016; 51:8–12. [PubMed: 26711689]
8. Esch EW, Bahinski A, Huh D. Organs-on-chips at the frontiers of drug discovery. Nature Reviews Drug Discovery. 2015; 14:248–260. [PubMed: 25792263]
9. Xinaris C, Brizi V, Remuzzi G. Organoid Models and Applications in Biomedical Research. Nephron. 2015; 130:191–199. [PubMed: 26112599]
10. Hynds RE, Giangreco A. Concise Review: The Relevance of Human Stem Cell-Derived Organoid Models for Epithelial Translational Medicine. STEM CELLS. 2013; 31:417–422. [PubMed: 23203919]
11. Lancaster MA, Knoblich JA. Generation of cerebral organoids from human pluripotent stem cells. Nature Protocols. 2014; 9:2329–2340. [PubMed: 25188634]
12. Eiraku M, et al. Self-organized formation of polarized cortical tissues from ESCs and its active manipulation by extrinsic signals. Cell Stem Cell. 2008; 3:519–532. [PubMed: 18983967]
13. Mariani J, et al. Modeling human cortical development in vitro using induced pluripotent stem cells. Proc Natl Acad Sci USA. 2012; 109:12770–12775. [PubMed: 22761314]
14. Lancaster MA, et al. Cerebral organoids model human brain development and microcephaly. Nature. 2013; 501:373–379. [PubMed: 23995685]
15. Eiraku M, et al. Self-organizing optic-cup morphogenesis in three-dimensional culture. Nature. 2011; 472:51–56. [PubMed: 21475194]
16. Caiazzo M, et al. Defined three-dimensional microenvironments boost induction of pluripotency. Nature Materials. 2016; 15:344–352. [PubMed: 26752655]
17. Warmflash A, Sorre B, Etoc F, Siggia ED, Brivanlou AH. A method to recapitulate early embryonic spatial patterning in human embryonic stem cells. Nature Methods. 2014; 11:847–854. [PubMed: 24973948]
18. Oh SKW, et al. Long-term microcarrier suspension cultures of human embryonic stem cells. Stem Cell Research. 2009; 2:219–230. [PubMed: 19393590]
19. Molander H, Olsson Y, Engkvist O, Bowald S, Eriksson I. Regeneration of peripheral nerve through a polyglactin tube. Muscle & Nerve. 1982; 5:54–57. [PubMed: 7057806]
20. Chenn A, Walsh CA. Regulation of Cerebral Cortical Size by Control of Cell Cycle Exit in Neural Precursors. Science. 2002; 297:365–369. [PubMed: 12130776]
21. Subramanian L, Remedios R, Shetty A, Tole S. Signals from the edges: The cortical hem and antihem in telencephalic development. Seminars in Cell & Developmental Biology. 2009; 20:712–718. [PubMed: 19446478]
22. Miller JA, et al. Transcriptional landscape of the prenatal human brain. Nature. 2014; 508:199–206. [PubMed: 24695229]
23. Rakic P. Specification of cerebral cortical areas. Science. 1988; 241:170–176. [PubMed: 3291116]
24. Jones EG, Rakic P. Radial Columns in Cortical Architecture: It Is the Composition That Counts. Cereb Cortex. 2010; 20:2261–2264. [PubMed: 20667930]

25. Geschwind DH, Rakic P. Cortical Evolution: Judge the Brain by Its Cover. Neuron. 2013; 80:633–647. [PubMed: 24183016]
26. Kadoshima T, et al. Self-organization of axial polarity, inside-out layer pattern, and species-specific progenitor dynamics in human ES cell-derived neocortex. Proc Natl Acad Sci USA. 2013; 110:20284–20289. [PubMed: 24277810]
27. Paşca AM, et al. Functional cortical neurons and astrocytes from human pluripotent stem cells in 3D culture. Nature Methods. 2015; 12:671–678. [PubMed: 26005811]
28. Qian X, et al. Brain-Region-Specific Organoids Using Mini-bioreactors for Modeling ZIKV Exposure. Cell. 2016; 165
29. Sievers J, Pehlemann FW, Gude S, Berry M. Meningeal cells organize the superficial glia limitans of the cerebellum and produce components of both the interstitial matrix and the basement membrane. J Neurocytol. 1994; 23:135–149. [PubMed: 8195812]
30. Halfter W, Dong S, Yip Y-P, Willem M, Mayer UA. Critical Function of the Pial Basement Membrane in Cortical Histogenesis. J Neurosci. 2002; 22:6029–6040. [PubMed: 12122064]
31. Rakic P. Evolution of the neocortex: a perspective from developmental biology. Nature Reviews Neuroscience. 2009; 10:724–735. [PubMed: 19763105]
32. Wang X, Tsai J-W, LaMonica B, Kriegstein AR. A new subtype of progenitor cell in the mouse embryonic neocortex. Nat Neurosci. 2011; 14:555–561. [PubMed: 21478886]
33. Marín O, Valiente M, Ge X, Tsai L-H. Guiding Neuronal Cell Migrations. Cold Spring Harb Perspect Biol. 2010; 2:a001834–a001834. [PubMed: 20182622]
34. Otani T, Marchetto MC, Gage FH, Simons BD, Livesey FJ. 2D and 3D Stem Cell Models of Primate Cortical Development Identify Species-Specific Differences in Progenitor Behavior Contributing to Brain Size. Cell Stem Cell. 2016; 18:467–480. [PubMed: 27049876]
35. Matsuda T, Cepko CL. Electroporation and RNA interference in the rodent retina in vivo and in vitro. Proc Natl Acad Sci USA. 2004; 101:16–22. [PubMed: 14603031]
36. Villefranc JA, Amigo J, Lawson ND. Gateway compatible vectors for analysis of gene function in the zebrafish. Dev Dyn. 2007; 236:3077–3087. [PubMed: 17948311]
37. Mátés L, et al. Molecular evolution of a novel hyperactive Sleeping Beauty transposase enables robust stable gene transfer in vertebrates. Nat Genet. 2009; 41:753–761. [PubMed: 19412179]
38. Daza RAM, Englund C, Hevner RF. Organotypic slice culture of embryonic brain tissue. CSH Protoc. 2007; 2007 pdb.prot4914.
39. Li H, Durbin R. Fast and accurate short read alignment with Burrows-Wheeler transform. Bioinformatics. 2009; 25:1754–1760. [PubMed: 19451168]
40. Trapnell C, Pachter L, Salzberg SL. TopHat: discovering splice junctions with RNA-Seq. Bioinformatics. 2009; 25:1105–1111. [PubMed: 19289445]
41. Trapnell C, et al. Transcript assembly and quantification by RNA-Seq reveals unannotated transcripts and isoform switching during cell differentiation. Nat Biotechnol. 2010; 28:511–515. [PubMed: 20436464]
42. Roberts A, Trapnell C, Donaghey J, Rinn JL, Pachter L. Improving RNA-Seq expression estimates by correcting for fragment bias. Genome Biol. 2011; 12:R22. [PubMed: 21410973]
43. Love MI, Huber W, Anders S. Moderated estimation of fold change and dispersion for RNA-seq data with DESeq2. Genome Biol. 2014; 15:31.

Europe PMC Funders Author Manuscripts

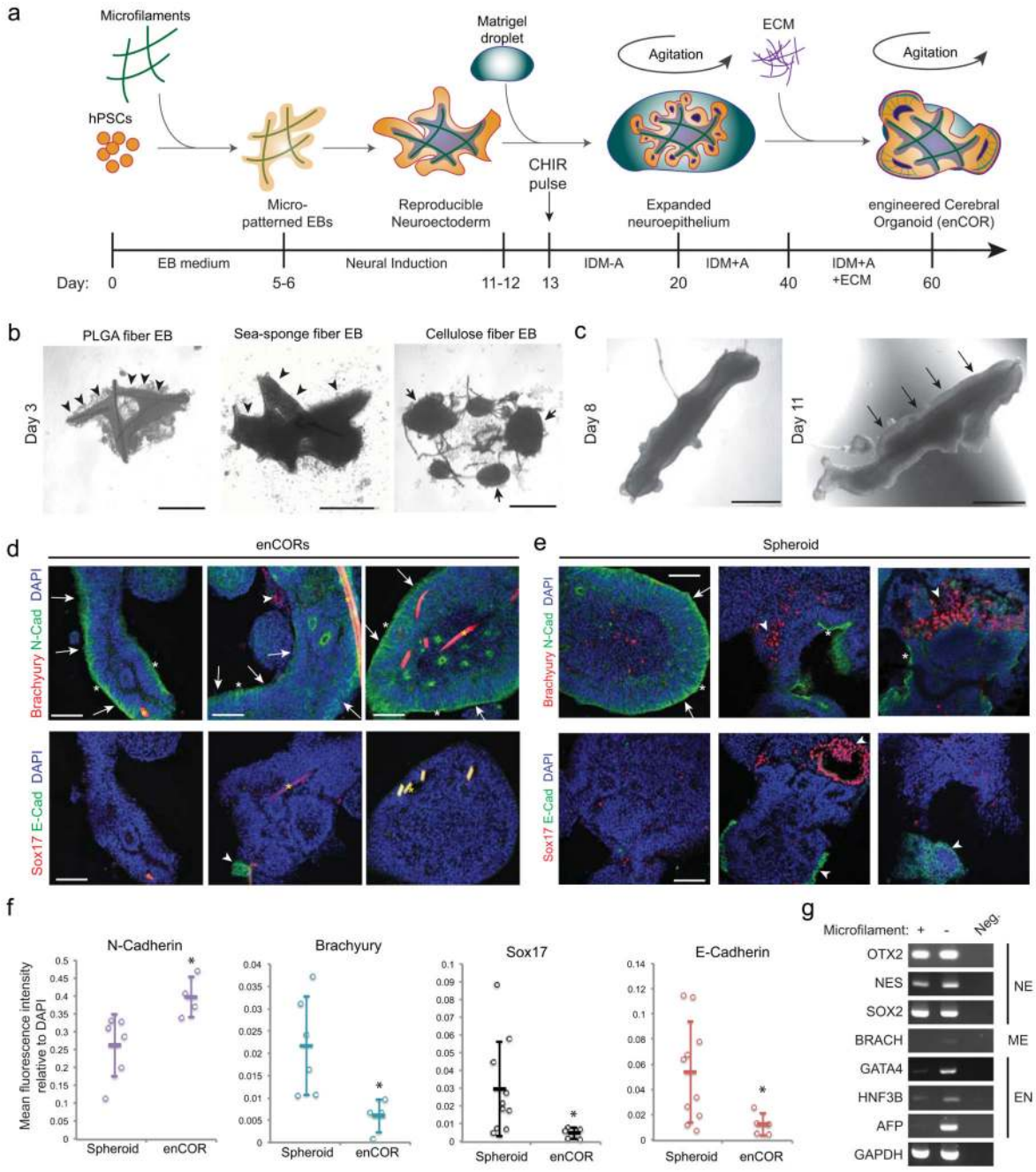


**Figure 1. Engineered cerebral organoids reproducibly generate elongated neuroepithelium**

**a.** Schematic of the method for generating engineered cerebral organoids (enCORs). Timeline and media used (methods) are shown at the bottom. Specific timing should be tailored to the developing morphology of the tissue as detailed in methods. **b.** PSCs attach to and coat the PLGA microfilaments (left panel, arrowheads) as well as fibers derived from sea-sponge (middle panel), whereas cellulose fibers with similar dimensions (right panel) fail to form elongated EBs at day 3 with H9 cells, and instead remain as clumps (arrows) only partially attached to the fibers. **c.** Bioengineered EBs from H9 cells at two time points,

day 8 and 11, during neural induction, showing clearing along the edges and polarized neural ectoderm (arrows). **d.** Immunohistochemical staining of day 10 bioengineered H9 EBs for the germ layer markers Brachyury for mesoderm, N-Cadherin for neural ectoderm, Sox17 for endoderm, and E-Cadherin for non-neural epithelium. Note the prevalence of polarized neural epithelia (arrows) displaying the apical domain on the surface (white asterix) with only occasional other germ layer identities (arrowhead). The microfilament can be seen as an autofluorescent rod (yellow asterix). **e.** Immunohistochemical staining of day 10 H9 spheroids for the same germ layer markers. Again, note the polarized neural epithelia (arrows) displaying the apical domain on the surface (white asterix) on an optimal brain organoid (upper left panel), while extensive mesoderm and endoderm identities (arrowheads) are visible in suboptimal organoids. **f.** Quantification of fluorescence staining of the above markers (mean grey value relative to DAPI). Dot-plot, mean ± SD. *$P$<0.05, Student's two-tailed $t$-test, n = 6-10 spheroids (10-day, H9), n = 4 enCOR organoids (10-day, H9). **g.** RT-PCR for expression of markers of the three germ layers: Neuroectoderm (NE), mesoderm (ME), and endoderm (EN) in 20-day microfilament organoids and organoids lacking a filament (spherical organoids) both made from H9 cells. Neg. is the negative water control. Images are cropped from full length gels shown in Supplementary Fig. 3b. Scale bars: 500 μm in b., 250 μm in c., 100 μm in d., e.

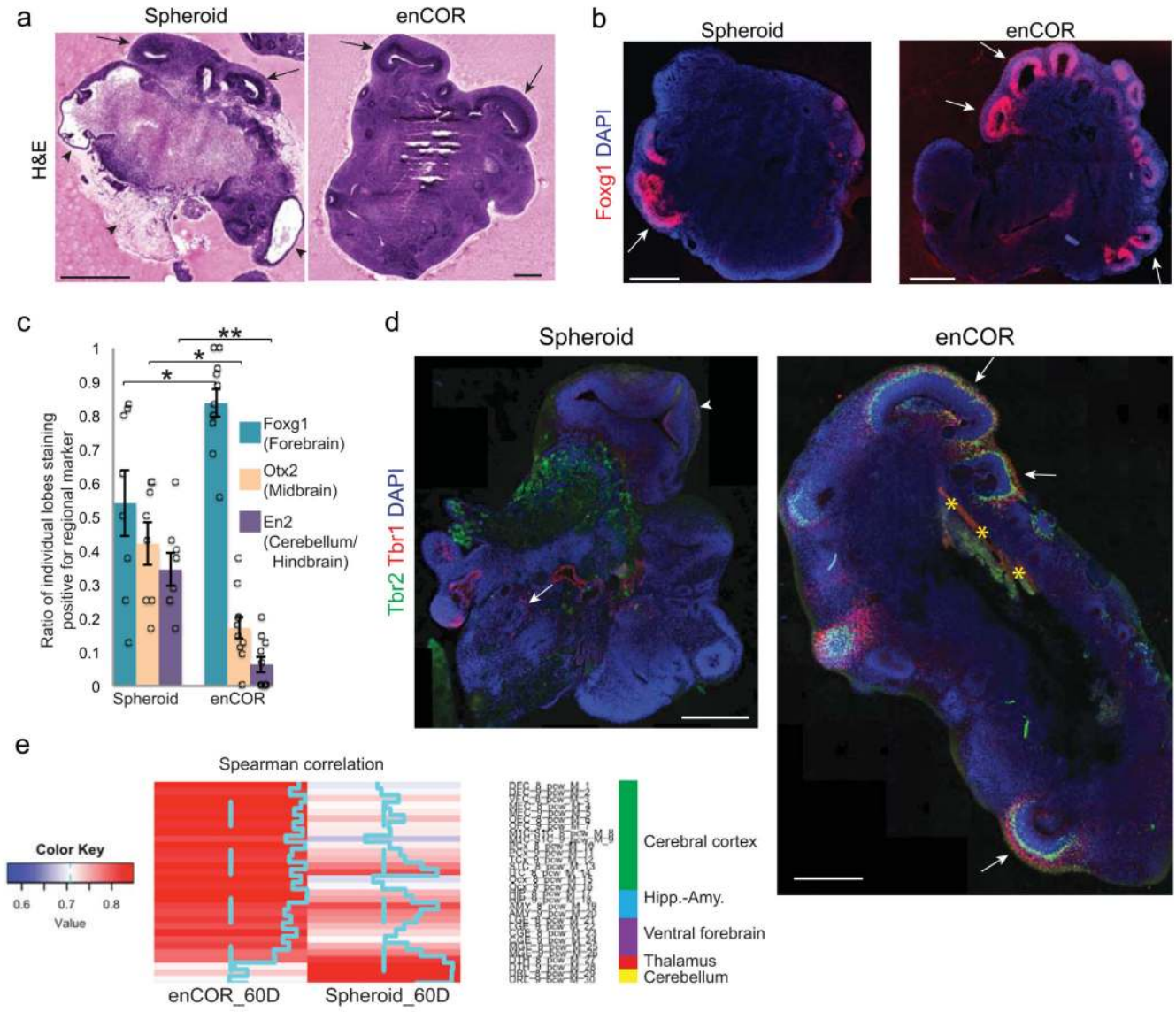


**Figure 2. enCORs show increased forebrain identity**

**a.** Haematoxylin and eosin (H&E) staining of representative 40-day spherical and enCOR organoids from H9 cells. Spheroids contain lobes of brain tissue (arrows) but also non-neural regions such as fluid-filled cysts and fibrous regions (arrowheads). enCORs instead contain pure neural tissue and many large continuous lobes of brain tissue (arrows). **b.** Representative sections of whole 40-day H9 organoids stained for the forebrain marker Foxg1. enCORs display increased numbers of Foxg1+ lobes (arrows) compared with spheroids. **c.** Quantification of the mean ratio of individual lobes displaying positive staining for the specified regional markers (see Supplementary Fig. 4e for representative stained sections). Foxg1 positive regions represent forebrain, regions highly positive for Otx2 represent midbrain, En2 positive regions represent cerebellar or hindbrain identities. Error bars are S.E.M. *$P$<0.01, **$P$<0.0001, Student's two-tailed $t$-test, n = 8 spheroids (40-day, H9) from three independent batches, n = 11 enCOR organoids (40-day, H9) from four




Europe PMC Funders Author Manuscripts

independent batches. **d.** Staining of day 40 H9 enCOR brain organoids and spheroids for the markers of dorsal cortex Tbr1 and Tbr2 reveals large lobes of tissue that are dorsal cortex (arrows) in enCORs. Spheroids show much fewer dorsal regions and some large brain regions that lack this identity (arrowhead). **e.** Heatmap of Spearman correlation coefficients of differentially expressed genes at 60 days in H9 spheroids and enCORs with the Allen BrainSpan transcriptome22. All brain regions are shown for stage I (8-9 post-conception weeks, see Supplementary Fig. 7c), sorted by anterior-posterior regional identity. Scale bars: 500 μm in a., b., d.



Europe PMC Funders Author Manuscripts

Europe PMC Funders Author Manuscripts

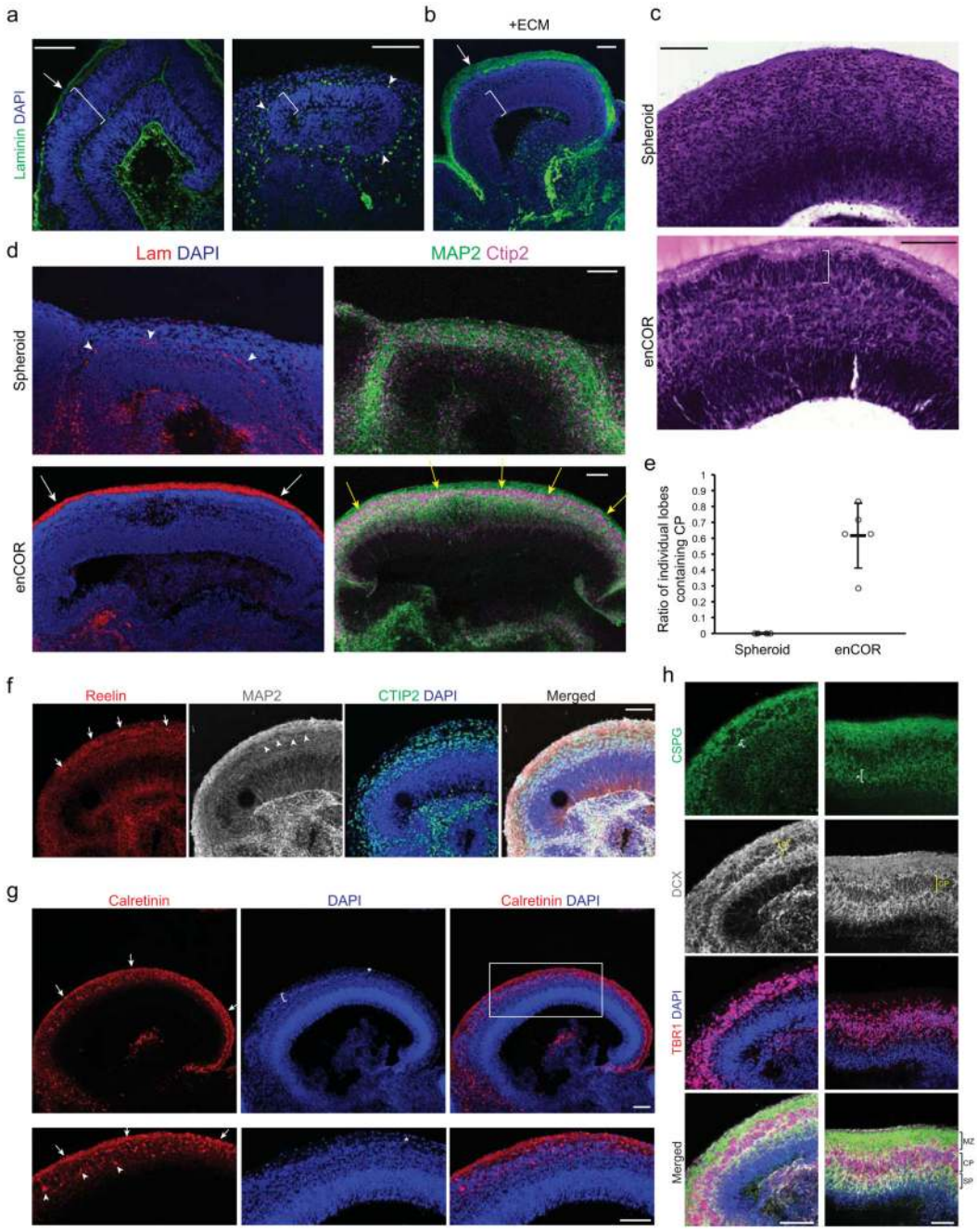


**Figure 3. enCORs with reconstituted basement membrane form cortical plate**

**a.** Staining for the basement membrane component laminin (green) in a day 48 H9 spheroid. Note the presence of the basement membrane surrounding a region of early neuroepithelium before the generation of neurons (first panel, arrow), whereas another, more developed region displays neuron generation and only sparse laminin labeling remains (arrowheads) adjacent to the ventricular zone (VZ, brackets) rather than over the surface of the organoid. **b.** Laminin staining of a 60-day H9 enCOR following treatment with dissolved extracellular matrix (ECM) in the form of Matrigel. Note the presence of a laminin-rich basement

membrane covering the surface of the organoid (arrow) and outside both the VZ (bracket) and newly generated neurons. **c.** Histological staining by H&E reveals the presence of a radially oriented dense CP (bracket) in enCORs with ECM, in contrast to the disorganized neurons of a spheroid. Both are 60-day H9 derived organoids. **d.** Immunohistochemical staining for laminin and the neuronal markers MAP2 and Ctip2 in day-60 H9 spheroid and enCOR. Note the presence of remnant basement membrane in the spheroid (arrowheads), whereas in the enCOR with ECM a basement membrane (white arrows) forms outside the dense Ctip2+ cortical plate (yellow arrows). **e.** Quantification of the mean ratio of individual lobes displaying a CP in H&E stained sections of day-60 H9 organoids. Individual lobes were identified by the presence of a ventricular space and radial VZ. CP was identified by the presence of a condensed band separated from the VZ by a cell-sparse zone. Each point is an independent batch of 2-3 organoids, each with several lobes of brain tissue. n = 4 independent batches of 12 spheroids, n = 5 independent batches of 12 enCORs. Mean across batches shown ± SD. **f.** Staining for Reelin in a dorsal cortical region early in CP formation (day-56 H9 enCOR). Several cells, which are strongly reactive for Reelin (arrows), localize outside the newly forming CP (arrowheads, recognizable by the lower intensity Map2 staining), consistent with Cajal-Retzius identity. Staining can also be seen more diffusely, consistent with its secreted role. **g.** Staining for calretinin, another marker of Cajal-Retzius cells, in a day-53 H9 enCOR, labels cells outside (arrows) the newly forming CP. Note the gradient of CP formation with more advanced CP to the left (bracket), and the initiation to the right (asterisk). Where the CP is further developed, one can also observe calretinin+ cells internal (arrowheads) to the CP, consistent with preplate splitting, and interneuron identity. **h.** Staining for chondroitin sulfate proteoglycan (CSPG) in day-68 H9 enCORs further demonstrates preplate splitting. Panels on the left show a less developed CP (yellow brackets) with the initiation of splitting and SP formation (white brackets with asterisk), while panels on the right show a more developed CP with layers consistent with SP, CP, and MZ. Scale bars: 100 μm in all panels.

Europe PMC Funders Author Manuscripts

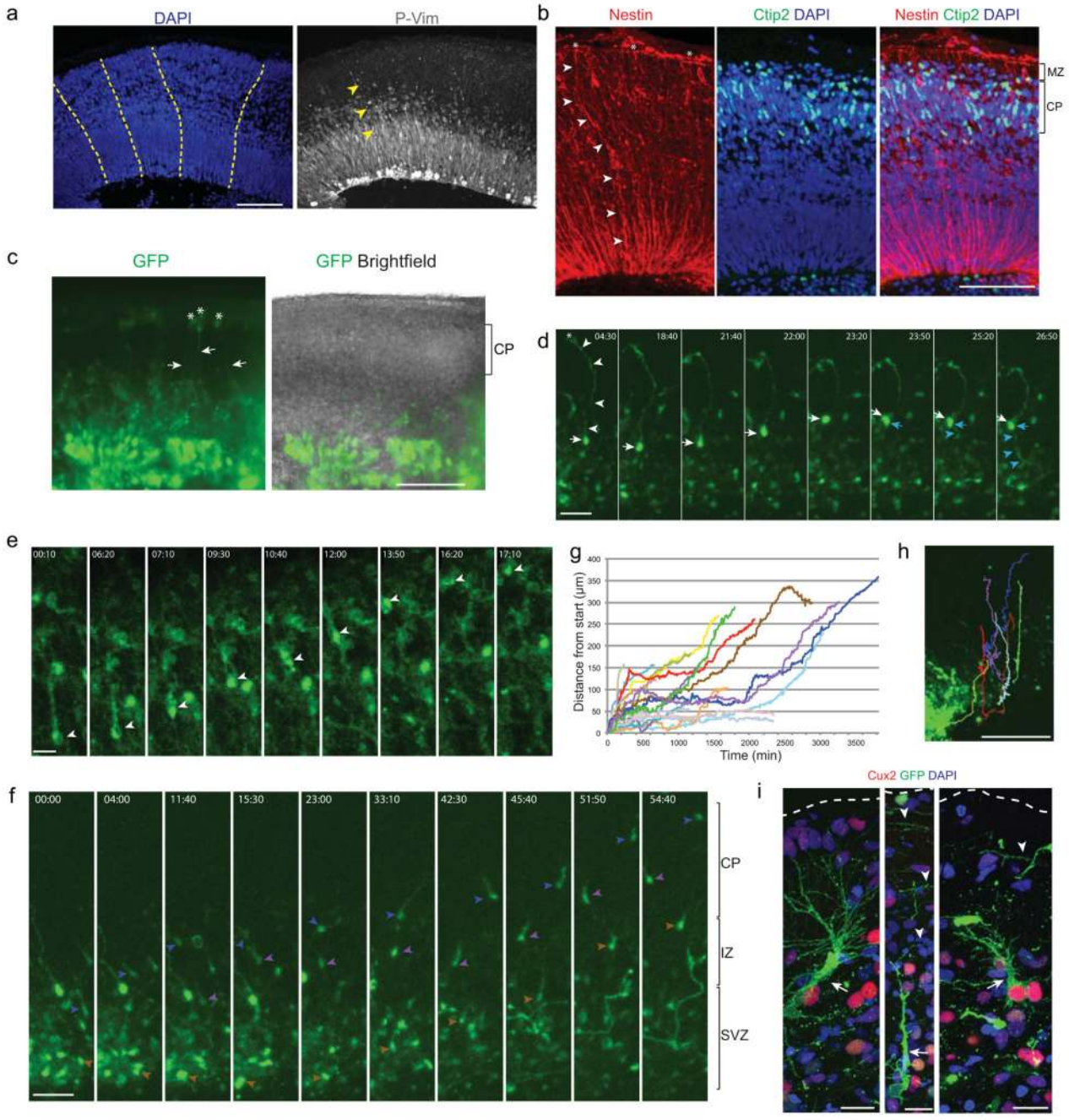


**Figure 4. enCORs display radial units and radial neuronal migration.**

**a.** Nuclear staining by DAPI in a 60-day H9 enCOR reveals radially organized units (dashed lines) while sparse staining for radial glial fibers with the marker of mitotic radial glia phosphorylated vimentin reveals fibers that extend the width of the tissue (arrowheads) reminiscent of a radial scaffold. **b.** Nestin staining for radial glia in day-70 H1 enCORs reveals long basal processes (arrowheads) that terminate with end feet at the surface of the organoid (asterisks) outside the CP and MZ. **c.** Electroporation of the VZ of a 64-day H9 enCOR with a GFP construct and vibratome sectioning the next day reveals individual RG

basal processes (arrows) that extend to the outer surface (asterisks). **d.** Frames from live imaging of an outer/basal RG (arrow marks the cell body) in a H1 enCOR electroporated with GFP on day 63, followed by vibratome sectioning four days later and live imaging 24-hours later (Supplementary Video 1). Note the long basal process (arrowheads) and endfoot (asterisk) as well as a division event including mitotic somal translocation beginning at 21:40. The newly generated daughter cell (blue arrow) then extends a process apically (blue arrowheads). Time stamp is hours:minutes. **e.** Frames from live imaging (Supplementary Video 5) of a membrane targeted farnesyl-GFP labeled neuron (arrowhead) showing radial migration into the CP. Time stamp is hours:minutes. **f.** Live imaging of migration of several neurons (arrowheads) in the same sample as d., displaying typical radial migration including transient stalling with multipolar morphology (for example blue arrowhead 11:40 to 23:00). Stills taken from Supplementary Video 1. Colors of the arrowheads match traces shown in g. and h. Time stamp is hours:minutes. **g.** Traces of distance traveled of 22 individual neurons from Supplementary Videos 1, 2, and 4. Colors of the traces match those shown in h. Note the characteristic transient stalling in several of the traces (red, blue, purple) with shorter duration stalling in the green and brown traces, while the light blue trace is already stalled at the start of the movie. **h.** Movement traces of individual neurons quantified in g. and shown in f. showing the movement into the intermediate zone with stalling and subsequent movement into the CP. **i.** Individual neurons labeled by electroporation of an H9 enCOR at day 64 with an integrating farnesylated GFP construct to allow for long-term labeling and analysis after 36 days. Note the primary dendrite extending from the cell body (arrows) toward the outer surface (dashed lines), as well as many parallel fibers (arrowheads) in the outer MZ. Scale bars: 100 μm in a., b., c., h., 50 μm in d., f., 20 μm in e., i.



Europe PMC Funders Author Manuscripts